Available online at www.sciencedirect.com
ScienceDirect
Trans. Nonferrous Met. Soc. China 32(2022) 2253−2265
Transactions of Nonferrous Metals Society of China
www.tnmsc.cn

Alloying behavior and characterization of $(CoCrFeNiMn)_{90}M_{10}$ (M=Al, Hf) high-entropy materials fabricated by mechanical alloying

Nai-ran WANG[1], Shou-ren WANG[2], Xiao-xiang GOU[1], Ze-cheng SHI[1], Jian-xiang LIN[1], Guo-qiang LIU[1], Yan WANG[1]

1. School of Materials Science and Engineering, University of Jinan, Jinan 250022, China;
2. School of Mechanical Engineering, University of Jinan, Jinan 250022, China

Received 28 June 2021; accepted 29 December 2021

Abstract: The alloying behavior and microstructures of the $(CoCrFeNiMn)_{90}M_{10}$ (M=Al, Hf) high-entropy alloy (HEA) powders fabricated by mechanical alloying were studied. The $CoCrFeNiMn)_{90}Al_{10}$ powders have duplex solid-solution structures. In contrast, nanocrystalline $HfNi_3$ anchoring in amorphous structures is found in the $(CoCrFeNiMn)_{90}Hf_{10}$ powders. The $(CoCrFeNiMn)_{90}Al_{10}$ powders show better ferromagnetic behaviors, mainly explained by the facilitated motion of the magnetic domain induced by the coherent interface between duplex phases. Combined with our previous work, the rules of forming solid-solution and amorphous phase in as-milled HEA powders are preliminarily proposed. It is found that, compared with the as-cast HEA reported previously, the variation range of mixing enthalpy with atomic size difference of the solid-solution formed in as-milled HEA powders is broader. Moreover, the variation ranges between mixing enthalpy and entropy with atomic size difference of the amorphous phase in HEA powder become wider than those of high-entropy bulk metallic glass.

Key words: high-entropy powder; mechanical alloying; ferromagnetic properties; alloy design; phase stability

1 Introduction

High-entropy alloys (HEAs) have witnessed fast development as novel multi-component alloys with solid solution structures. Their unique physical, chemical, and excellent mechanical properties have stimulated extensive research in the field of materials science [1−3]. Ingot metallurgy is still the primary processing strategy to generate HEAs in most reported works. However, the arc-melt/casting methods have some disadvantages, such as phase segregation, inhomogeneous microstructure, limited shape and size of final products [4]. More recently, as an exciting alternative, powder metallurgy is beneficial to introducing nanostructures and improving HEA capabilities [5]. The fabrication and structure/properties of the pre-alloyed HEA powders (i.e., the starting materials) have also been a significant concern. In addition, the HEA powders have been formulated in ink with improved printability in 3D printing HEA products [6,7]. Mechanical alloying (MA) is the most common method to obtain alloy powders, with the advantages of enabling flexible and optimal composition and phase structure design under reasonable alloying time and energy input. Moreover, MA has been considered as one of the powerful processing methods for preparing a wide variety of HEA powders [8−10]. For example, CoCrFeNiW and $CoCrFeNiW_{0.5}Mo_{0.5}$ HEA powders have been prepared by MA, showing body-centered cubic (BCC) and face-centered cubic (FCC) solid solution phases. These HEA coatings fabricated by vacuum hot-pressing sintering showed remarkable wear and corrosion resistance [9]. The as-milled CuZrNiAlTiW powders were used as a reinforcement to prepare Al-based composite, exhibiting decent

Corresponding author: Yan WANG, Tel: +86-531-82765473, Fax: +86-531-87974453, E-mail: mse_wangy@ujn.edu.cn
DOI: 10.1016/S1003-6326(22)65945-4

compression properties with high yield strength and good plasticity [10].

Combined with the excellent application perspective of HEA powders, their composition design obtained through MA is very critical. Furthermore, it is urgent to predict phase structures of the as-milled HEA powders with given principal elements.

The design of HEA alloys can be rationalized by statistically analyzing parameters of the atomic size difference of elements (δ), mixing enthalpy (ΔH_{mix}), mixing entropy (ΔS_{mix}), electronegativity difference, and valence electron concentration (VEC) [11,12]. The Ω is also a valid indicator, defined as the mixing entropy timing the average melting temperature of the elements over the mixing enthalpy [13]. It is necessary to point out that the definitions of these parameters only provide valuable guidance for the as-cast HEAs. However, the prediction of the phase stability for as-milled HEA powders has not been systematically studied. Thus, it is significant and necessary to propose a scientific scheme predicting the phase structure (e.g., solid solution or amorphous structure) in HEA powders.

In this work, the microstructural evolution and magnetic properties of $(CoCrFeNiMn)_{90}Al_{10}$ and $(CoCrFeNiMn)_{90}Hf_{10}$ (denoted as Al10 and Hf10, respectively) HEA powders fabricated by MA were investigated systematically. The compositional design of Al10 and Hf10 alloys was developed based on the prototype of classic CoCrFeNiMn HEA with a single FCC solid solution fabricated by casting [14] and MA [15]. Several studies showed that adding elements into HEAs could substantially affect the crystalline structure, microstructural morphology, and subsequent properties [16−18]. It is interesting to probe the effects of Al and Hf addition on the alloying behavior and properties of as-milled CoCrFeNiMn-based HEA powders. Meanwhile, combined with our previous work, the phase stability prediction of the as-milled powders under similar MA conditions was explored.

2 Experimental

The raw powders of Co, Cr, Fe, Ni, Mn, Al, and Hf powders (≥99.5 wt.%, ≥75 μm with nominal compositions of $(CoCrFeNiMn)_{90}Al_{10}$ and $(CoCrFeNiMn)_{90}Hf_{10}$ were processed by a high-energy planetary ball mill at room temperature in an Ar atmosphere. Table 1 lists the characteristic parameters of tested elements and nominal compositions used in this work. The stainless ball-to-powder (10, 5, and 2 mm in diameter) mass ratio was 15:1 in stainless steel vial, and the rotation speed of the central disc was 350 r/min. The milling procedure was interrupted every 30 min and then held for 10 min to avoid increasing the vial temperature. In addition, about 0.5 g of as-milled product was taken out of the vial at different interruption time for further analysis and characterization.

Table 1 Characteristic parameters and nominal compositions of elements used in this work

Element	Atomic radius/Å	Melting temperature/°C	Lattice structure	Nominal composition/at.%
Co	1.251	1495	HCP	18
Cr	1.249	1907	BCC	18
Fe	1.241	1538	BCC	18
Ni	1.246	1453	FCC	18
Mn	1.35	1241	BCC	18
Al	1.432	660	FCC	10
Hf	1.578	2233	HCP	10

HCP: Hexagonal close packed

Structural and microstructural characterization of the as-milled powders was performed by X-ray diffraction (XRD, Rigaku D8 Advance) in the Bragg−Brentano geometry using Cu K_α radiation (λ=0.15406 nm), field-emission scanning electron microscopy (FESEM, QUANTA FEG 250) equipped with energy-dispersive spectrometry (EDS), and transmission electron microscopy (TEM, JEM−2100) coupled with selected area electron diffraction (SAED) and high-resolution transmission electron microscopy (HRTEM). An alternating gradient magnetometer (AGM) was employed to evaluate the magnetic properties of the as-milled powders. The saturation magnetization (M_s) and coercivity (H_c) were determined at room temperature using a maximum applied field of 6.36×10^5 A/m.

3 Results and discussion

3.1 Structural characterization

Figure 1 presents the XRD patterns of Al10

and Hf10 HEA powders at various milling time. The characteristic parameters obtained from XRD patterns versus milling time are shown in Fig. 2. The diffraction peaks of raw metal elements are presented at 0 h-milled Al10 samples (Fig. 1(a)). After 10 h, the diffraction peaks shift to a lower angle and their intensities dramatically decrease. In addition to the Co peak at 2θ=76.4°, some diffraction peaks disappear or overlap at high angles ($2\theta > 75°$), suggesting the solid solution formation. Cold welding and crushing circulation promote mutual dissolution between different elements during the milling process and facilitate the alloying reaction. When the milling time extends from 20 to 40 h, some Co, Ni, and Mn peaks disappear. The solid solution behavior of Al10 powders becomes distinct. After 80 h, the milling products have a duplex FCC + BCC structure. Moreover, 120 h MA results in no noticeable change except for the appearance of minor broadened peaks of solid solution. As indicated by the peak profile in the inset of Fig. 1(a),

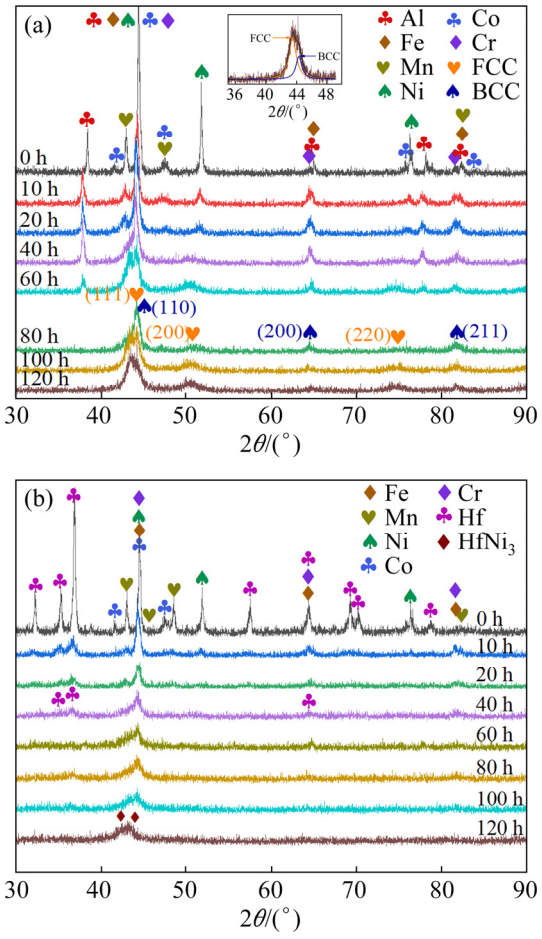

Fig. 1 XRD patterns of Al10 (a) and Hf10 (b) HEA powders after different milling time

the deconvolution of prominent diffraction peaks, which belong to FCC and BCC phases, suggests the presence of FCC and BCC phases. According to Ref. [15] reported earlier, the CoCrFeNiMn powders derived from MA own a single FCC phase. In the $(FeCoNiCrMn)_{100-x}Al_x$ HEA system, the as-cast structure tends to evolve from the initial FCC ($x < 8$) to a mixture of FCC + BCC duplex phases (x=8−16) and then a single BCC structure ($x > 16$) with the increase of Al contents [18]. Al atom with a larger radius than the other principal metals in this system caused an apparent lattice straining effect. Therefore, the excessive addition of Al induced the transition from a close-packed FCC to a loose-packed BCC structure, so that the lattice distortion energy was relaxed [19].

The phase constitution evolution of the Hf10 sample at different MA time is shown in Fig. 1(b). The crystalline peaks of each principal element are observed at 0 h. Different from Al10 powder, all the diffraction peaks of Hf10 sample shift to a higher angle after 10 h milling. Interestingly, the intensity of diffraction peaks decreases vastly, and some Co and Mn peaks almost disappear. Only Hf peaks are retained with extending milling time to 40 h, except for a major diffusion peak at $2\theta \approx 44°$. Since the MA process mainly involves mechanical crushing between powder particles and solid diffusion between elements, the element with a higher melting temperature has a smaller intrinsic diffusion coefficient, inducing the low alloying rate [20]. According to Table 1, Hf has the highest melting temperature of 2233 °C among the principal elements, exhibiting the slowest alloying rate during MA. So, other principal elements as solutes in Hf10 HEA tend to diffuse in Hf acting as a solvent. After 60 h, a pronounced smooth hump appears at $41° < 2\theta < 46°$, implying the amorphous phase formation. After 80 and 120 h, the as-milled product contains an amorphous phase except for less $HfNi_3$ intermetallic phase, which is also called HE amorphous alloy. It indicates that adding Hf with a much larger atomic size (1.578 Å) induces severer confusion of atomic arrangement and inhibits solid solution behavior between principal elements, promoting amorphous phase formation.

For further exploring the evolution of phase structure, the crystal parameters of as-milled Al10 were studied, as shown in Fig. 2(a). The main diffraction peak presents two inconspicuous

splitting characteristics after a solid solution reaction. Thus, the corresponding lattice parameters of the main peak cannot be calibrated accurately. The (200) peak of the FCC phase is chosen to calculate and compare the lattice parameters. The crystallite size (D) of FCC phase at different milling time is calculated by the Scherrer equation: $D=K\lambda/(\beta\cos\theta)$, where β is the full width at half maxima of the (200) peak, θ is the diffraction angle, K(=0.89) is a constant, and λ is the X-ray wavelength. It reveals that the D values become distinctly reduced with increasing milling time. The lattice constant (a) increases from 3.5265 Å of pure Ni phase (0 h) to 3.6249 Å of Ni-rich phase (60 h), then decreases to 3.5881 Å of 80 h-milled FCC solid solution, and finally increases to 3.6141 Å of 120 h-milled one. The lattice strain (η) values of the milled samples are obtained to identify the lattice distortion further, as shown in Fig. 2(a). Element Ni with an FCC structure exhibits Bragg peaks close to FCC-type solid solution in Al10 HEA. Accordingly, the lattice constant of the Ni element is selected as the unit cell parameter (a_0) of 3.5238 Å. The lattice strain (η) is expressed as $\eta=\Delta a/a_0$ ($\Delta a=|a-a_0|$). Following this equation, the values of η present a similar variation tendency with a. The largest η of 60 h-milled Al10 samples indicates that many metal elements are dissolved in Ni lattice (FCC phase), leading to the large lattice distortion. Moreover,

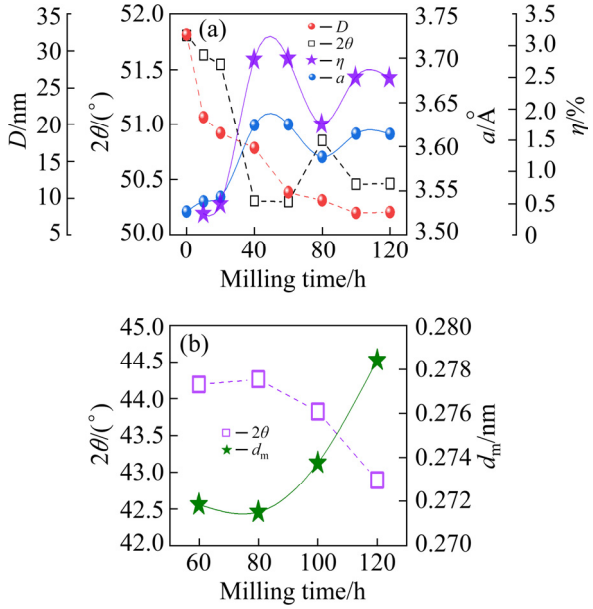

Fig. 2 Characteristic parameters obtained from XRD patterns for Al10 (a) and Hf10 (b) HEA powders at given milling time

the rise in grain boundary fractions and lattice deformation also cause the increased lattice distortion under suitable conditions of longer milling time. However, the decreased lattice distortion after the formation of dual solid solutions is attributed to the miscibility of all metal elements and the precipitation of the BCC phase from the FCC phase matrix.

The amorphous phase stably obtained for the Hf10 sample after the milling time of 60 h exists even increasing the milling time to 120 h. Figure 2(b) reveals the variation trend of the average nearest-neighbor atomic distance (d_m) in the amorphous phase at various milling time. The values of d_m are obtained by equation: $1.23\lambda=2d_m\sin\theta_1$, where θ_1 is the peak position corresponding to the first maximum peak on the XRD pattern, and 1.23 is the correction factor used for liquid and amorphous solid [21]. Overall, there is a clear upward trend of the d_m for the amorphous HEA with increasing milling time, except for a slight decrease in the 80 h-milled samples. The enhanced topological instability was characterized by the increased d_m [22]. It indicates that extending the milling time of the Hf10 amorphous powders leads to lattice expansion, which further induces the weakened topological stability.

3.2 Microstructures

Figure 3(a) shows that 10 h-milled All0 HEA powders are in irregular flat shapes with a larger aspect ratio. The difference in powder size is distinct, and larger powders are about 80 μm in length. However, the small ones only reach about 20 μm. Repeated fracturing and cold welding occur throughout the milling process, resulting in the continual refinement of the particles. The 80 h-milled powders become refined obviously. Increasing the MA time to 120 h, the large powder particles are further crushed, and the particle size difference decreases. From Fig. 4(a), the particle size distribution of 120 h-milled powders is almost nonsymmetric with three unimodal peak particle sizes. After calculation, the average size of 27.34 μm and median size of 22.76 μm are obtained.

In Fig. 3(d), the size distribution in Hf10 powders becomes significantly narrower than that of the as-milled Al10 sample after the same milling

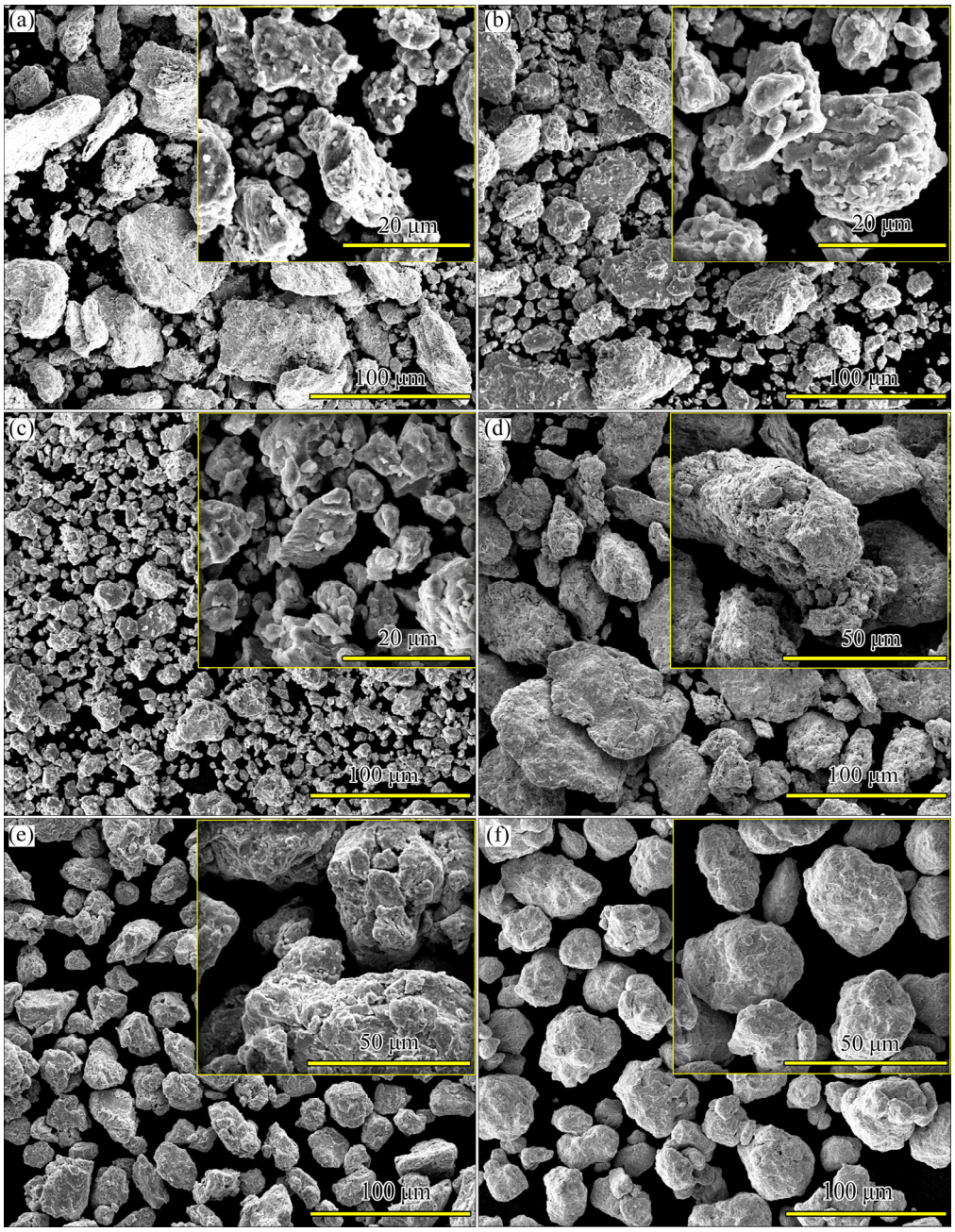

Fig. 3 FESEM images of Al10 (a−c) and Hf10 (d−f) HEA powders at different milling time: (a, d) 10 h; (b, e) 80 h; (c, f) 120 h

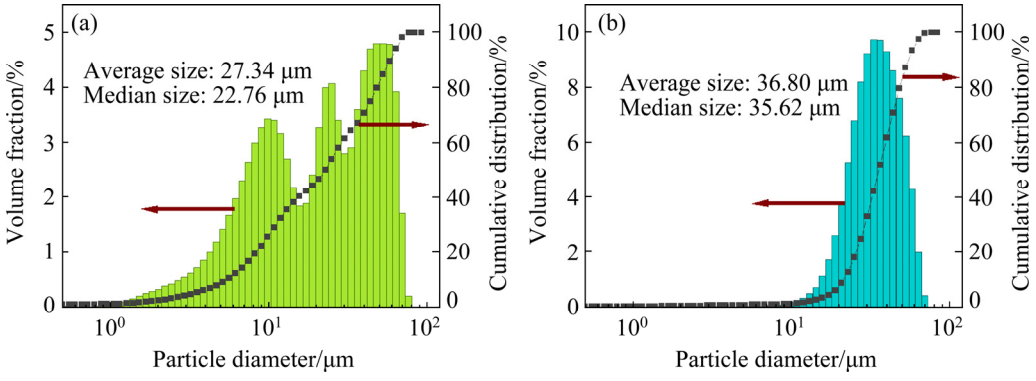

Fig. 4 Size distribution of Al10 (a) and Hf10 (b) HEA powders at milling time of 120 h

time of 10 h. This indicates that Hf can induce evident deformation and breakage for a mixture of powder particles of different elements. After alloying for 80 h (Fig. 3(e)) and 120 h (Fig. 3(f)), a homogeneous morphology is achieved with the balance of agglomeration, fracture, and size reduction. Meanwhile, the 120 h-milled Hf10 powders, mostly at 35 μm, exhibit uniform size distribution (Fig. 4(b)). The elemental powders experience breaking and welding to form HEA powder particles under the rotation of the grinding bowl during the milling process. When trapped between colliding balls, the particles of Al10 HEA (80−120 h) with more FCC phases are soft enough to undergo extensive plastic deformation and fracturing, resulting in flattening and cracking. On the contrary, the particles of amorphous Hf10 powders possessing fragile characteristics reveal the brittle fracture under the mechanical force, leading to the decreased and uniform particle size.

The chemical compositions of the Al10 and Hf10 HEA powders at different milling time are obtained by EDS analysis, as shown in Fig. 5. The molar fraction of each element in 10 h-milled powders is different from the nominal composition. Because the alloying reaction at this MA initial stage is relatively chaotic, and some elements begin to undergo solid solution successively, obviously such as Co element. Extending the milling time to 80 and 120 h at which the alloying reaction of the solid solution has completed, the MA state then becomes stable. Thus, the compositions of the stable milling products are nearly equal to the nominal composition, especially the latter. This indicates that the homogeneity degree of the components increases due to alloying solid solution behavior.

Moreover, it is interesting that, compared with the Al10 sample, the compositions of the Hf10 sample after these three different MA stages are close to the nominal composition. This suggests that Hf with a sizeable atomic size leads to a significant lattice distortion, further accelerating the alloying reaction. More considerable driving energy makes it easier for central atoms to diffuse, facilitating a more homogeneous state of components.

Figures 6 and 7 show TEM and HRTEM images, and the corresponding SAED patterns of 120 h-milled Al10 and Hf10 powders, respectively. Figure 6(a) demonstrates that black irregular particles with sizes less than 40 nm are distributed on the light gray matrix. The SAED patterns in Figs. 6((b) and (c)) of Al10 HEA are indexed to FCC structure and FCC + BCC structure for Regions I and II corresponding to the matrix and inlaid particle (marked by circles), respectively. In addition, the HRTEM image confirms a coherent interface between the FCC matrix and BCC particle (identified by the dotted box), revealing the compatibility of dual phases (FCC and BCC). The lattice fringe spacings of 0.2104 and 0.2045 nm agree nicely with the *d*-spacings of FCC (111) matrix and BCC (110) particles, respectively.

The TEM image in Fig. 7(a) reveals the microstructure of the Hf10 sample. The SAED pattern (Fig. 7(a-1)) obtained from Region I shows the diffuse halo pattern, and the corresponding HRTEM image (Fig. 7(b)) presents the isotropic mazelike-pattern, indicating the amorphous nature of the particles. In contrast, the dot pattern in the

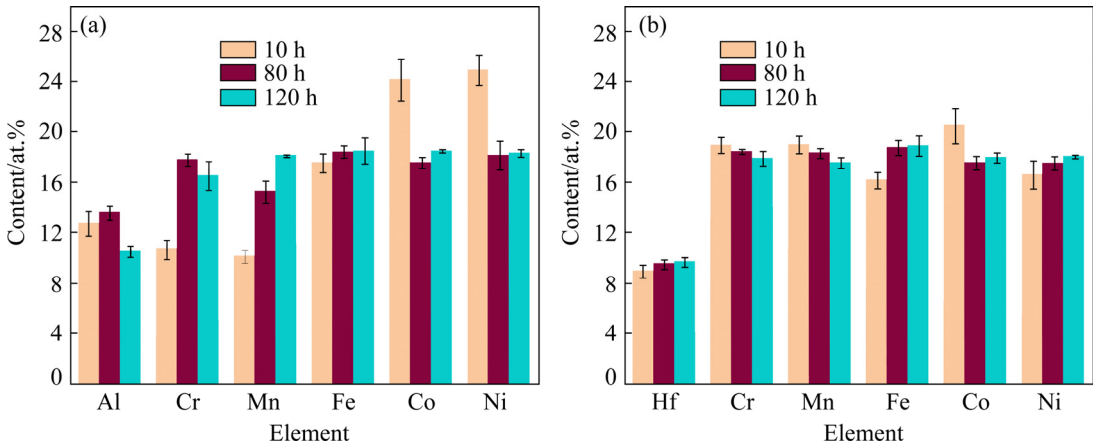

Fig. 5 Chemical compositions of Al10 (a) and Hf10 (b) HEA powders at different milling time according to EDS analysis

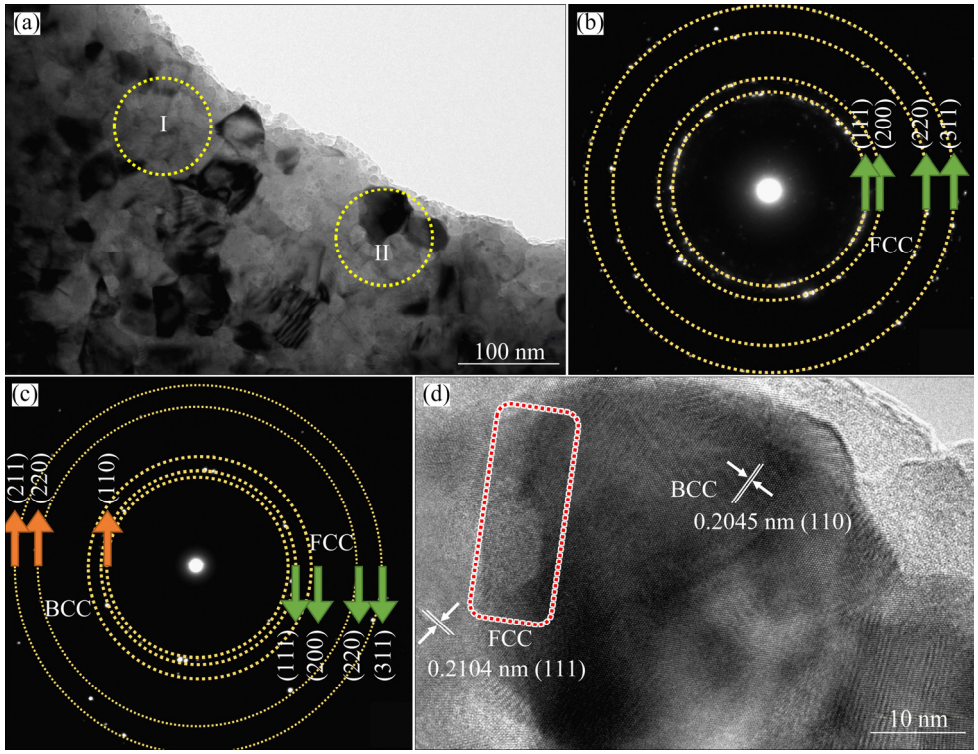

Fig. 6 TEM image of 120 h-milled Al10 HEA powders (a), SAED patterns corresponding to Regions I (b) and II (c) in (a), respectively, and HRTEM image (d) obtained from Region II in (a)

SAED image in Fig. 7(a-2) (collected from Region II, in Fig. 7(a)) confirms the nanocrystalline of the $HfNi_3$ intermetallic compound with an HCP structure. The associated HRTEM image from Fig. 7(c) also shows clear lattice fringes on the amorphous matrix. It is confirmed that a few nanocrystallines are precipitated from the amorphous phase after a long MA time, resulting in the loose atomic range of the amorphous matrix. Therefore, a larger d_m value is obtained for the 120 h-milled Hf10 powders.

3.3 Magnetic properties

Regarding the investigation of magnetic properties, Fig. 8 presents the plots of the hysteresis loops of 120 h-milled Al10 and Hf10 powders. The inset table summarized the parameters of magnetic properties. Both samples exhibit the ferromagnetic characteristic. The H_c values of as-milled Al10 and Hf10 samples are 11759 and 12165 A/m, respectively. The higher H_c could be derived from the growth of defects that contributed to the enhanced resistance to the demagnetization [23]. Moreover, the repetitive crushing and cold welding during a long milling time caused the milling-induced internal stress [24], raising the value of H_c.

The Al10 powders show a higher M_s of 20.52 $A \cdot m^2/kg$ than that of the Hf10 sample (10.25 $A \cdot m^2/kg$), reflecting the superiority of ferromagnetic properties. For FeCoNi-based HEAs, magnetic behaviors strongly depend on the addition of alloying elements, usually accompanying structural changes [25,26]. The paramagnetic properties in the FeCoNiCr alloy changed dramatically to ferromagnetism by adding the non-magnetic element Al [27]. Moreover, ZOU et al [28] reported that the FeCoNiCrMn HEA exhibited paramagnetic behavior with M_s of 0.5 $A \cdot m^2/kg$. In the present study, adding the non-magnetic elements Al and Hf, especially Al, to the as-milled CoCrFeNiMn HEA powders significantly enhances ferromagnetic properties. This is because the addition of Al to CoFeMnNi can reduce the number of down-spins of Mn, thus making the alloy behave ferromagnetically [28].

M_s is primarily determined by the composition and atomic-level structures and can be influenced by the phase composition of the alloys [29]. The as-milled Al10 powders have duplex FCC + BCC solid solution structures, while the Hf10 powders mainly possess an amorphous phase with a few nanocrystalline $HfNi_3$. The addition of Al induces

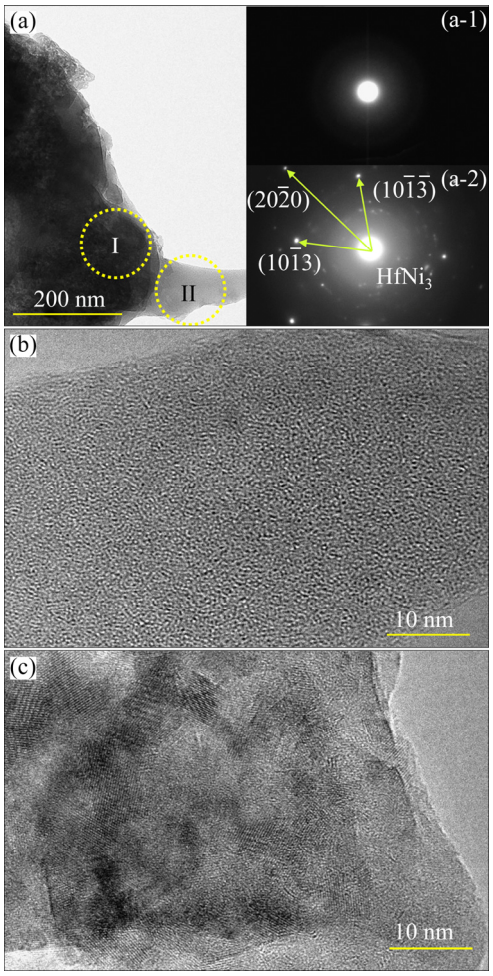

Fig. 7 TEM images of 120 h-milled Hf10 HEA powders (a), SAED patterns corresponding to Regions I (a-1) and II (a-2) in (a), respectively, and HRTEM images obtained from Regions I (b) and II (c), respectively

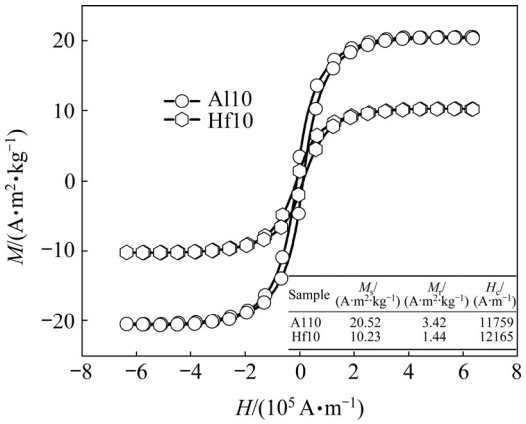

Fig. 8 Hysteresis loops of as-milled Al10 and Hf10 powders at milling time of 120 h, and magnetic parameters as inset table (M is magnetization, M_s is saturation magnetization, and M_r is remanence)

the BCC phase precipitated from the FCC matrix. According to TEM results (Fig. 6), the coherent interface between FCC and BCC phases with low interface energy observed in the Al10 sample facilitates the motion of the magnetic domain, which is beneficial to enhancing the ferromagnetic properties. Moreover, the precipitation of the $HfNi_3$ intermetallic compound in the Hf10 sample can act as a pinning point and block domain movement, impairing the improvement of M_s.

3.4 Statistics analysis of phase stability

In work reported previously, a series of parameters of δ, ΔH_{mix}, ΔS_{mix}, and VEC were used to characterize the collective behavior of the constituent elements in the multi-component alloys. These parameters were defined by Eqs. (1)−(4), respectively:

$$\delta = \sqrt{\sum_{i=1}^{n} c_i \left(1 - \frac{r_i}{\bar{r}}\right)^2} \tag{1}$$

where c_i and r_i are the molar fraction and atomic radius of the ith element, and $\bar{r}$ is the weighted average of atomic radius.

$$\Delta H_{mix} = \sum_{i=1, i\neq j}^{n} 4\Delta H_{mix}^{AB} c_i c_j \tag{2}$$

where ΔH_{mix}^{AB} is the mixing enthalpy of binary liquid AB alloys.

$$\Delta S_{mix} = -R\sum_{i=1}^{n} c_i \ln c_i \tag{3}$$

where R is the molar gas constant.

$$VEC = \sum_{i=1}^{n} c_i (VEC)_i \tag{4}$$

where $(VEC)_i$ is the VEC for the ith element.

The previous formation mechanisms were summarized for the conventional casting method of HEAs. However, the same HEAs synthesized by different routes possess different microstructures, resulting in different performances. The CoCrFeNiW HEA synthesized through arc melting consisted of FCC and μ phases [30]. However, when it was synthesized through MA, it consisted of FCC and BCC solid solutions [9]. Therefore, the synthesis route is vital for the HEA phase composition.

MA is one of the non-equilibrium processes to extend the solubility levels. The high energy from milling balls could be transferred to alloy powders during the milling process [31]. It is undoubtedly a concern that the milling products obtained by the

MA technique are not necessary in the equilibrium state. Therefore, the reported parameter ranges of phase formation criterion are not fully applicable to as-milled HEA powders. It is necessary to explore the new phase formation rules of solid solution or amorphous phase for the HEA powders fabricated by MA. Generally, the as-milled products mainly depend on the ball milling time, ball-to-powder mass ratio, vial and balls materials, and the central disc's rotation speed. Different ball milling processes can lead to different products. It is reasonable to compare the differences of the MA products under similar ball-milling conditions. Therefore, the tested HEA systems under similar MA conditions in our previous work are chosen as the research object to discuss the criteria. We calculated and summarized the corresponding parameters to verify the phase formation rules for as-milled HEA powders studied, as revealed in Table 2. This present work is expected to provide valuable guidance for developing solid solution or amorphous phases in HEA powders.

Table 2 Parameters of δ, ΔH_{mix}, ΔS_{mix}, VEC, and microstructure for as-milled HEA powders

As-milled powder	δ/%	ΔH_{mix}/(kJ·mol^{-1})	ΔS_{mix}/(J·mol^{-1}·K^{-1})	VEC	Microstructure
CoCrFeNi [32]	0.30	−3.75	11.53	8.25	FCC
CoCrFeNiCu [32]	1.03	3.20	13.38	8.80	FCC
CoCrFeNiW [9]	3.79	−2.88	13.38	7.80	BCC + FCC
CoCrFeNiMo [9]	3.66	−4.64	13.38	7.80	BCC + FCC
$CoCrFeNiW_{0.5}Mo_{0.5}$ [9]	3.73	−3.76	14.53	7.80	BCC + FCC
$(CoCrFeNiMn)_{90}Al_{10}$	4.91	−9.20	14.75	7.50	BCC + FCC
$(Ni_{40}Fe_{30}Co_{20}Al_{10})_{90}Ti_{10}$ [33]	6.20	−16.10	12.28	8.05	FCC
CuZrAlTiNiW [10]	8.55	−28.44	14.90	6.40	BCC
HfCrVW [34]	8.94	−4.75	11.53	5.25	BCC
$HfCrVWMo_{0.2}$ [34]	8.72	−4.49	12.57	5.29	BCC
$HfCrVWMo_{0.6}$ [34]	8.35	−4.05	12.95	5.35	BCC
HfCrVWMo [34]	8.02	−3.68	13.38	5.40	BCC
HfCrNbTa [34]	8.20	−4.00	11.53	5.00	BCC
HfCrNbTaAl [34]	7.33	−16.32	13.38	4.60	BCC
HfCrNbTaMo [34]	7.58	−4.92	13.38	5.20	BCC
HfCrNbTaTi [34]	7.38	−3.20	13.38	4.80	BCC
FeSiBAlNiCe[35]	23.06	−38.78	14.90	5.17	AP
$FeSiBAlNiCo_{0.2}$ [36]	16.4	−27.96	14.24	5.74	AP
$FeSiBAlNiCo_{0.4}$ [37]	16.1	−28.09	14.47	5.80	AP
$FeSiBAlNiCo_{0.6}$ [37]	15.8	−28.13	14.63	5.87	AP
$FeSiBAlNiCo_{0.8}$ [36]	15.57	−30.56	14.90	6.17	AP
FeSiBAlNi [38]	17.05	−28.00	13.38	5.60	AP
FeSiBAlNiNb [38]	16.87	−40.78	14.90	5.50	AP
FeSiBAlNiGd [39]	23.04	−43.00	14.90	5.17	AP
CuZrAlTi [39]	10.20	−33.75	11.53	7.00	AP
CuZrNiAlTi [40]	9.23	−41.28	13.38	6.40	AP
CuZrNiAlTiSi [41]	11.10	−54.00	14.90	6.00	AP
FeSiBAlNiC [35]	16.7	−27.72	14.63	5.67	AP+Si
FeSiBAlNiCo [42]	15.57	−30.56	14.90	6.17	AP+FeSi
FeSiBAlNiCu [42]	15.66	−21.78	14.90	6.50	AP+nanocrystalline
FeSiBAlNiAg [42]	17.06	−18.78	14.90	6.50	AP+FCC
$(CoCrFeNiMn)_{90}Hf_{10}$	7.78	−11.93	14.75	7.60	AP+nanocrystalline

To better reflect the three main factors governing the phase stability, ΔH_{mix}, δ, and ΔS_{mix} are superimposed, as shown in Figs. 9(a, b). For forming solid solution in powders, when the newly defined δ value is less than 8.94%, the corresponding ΔH_{mix} is in the range of −28.44 to 3.2 kJ/mol and ΔS_{mix} is in the range of 11.53 to 14.90 J/(mol·K).

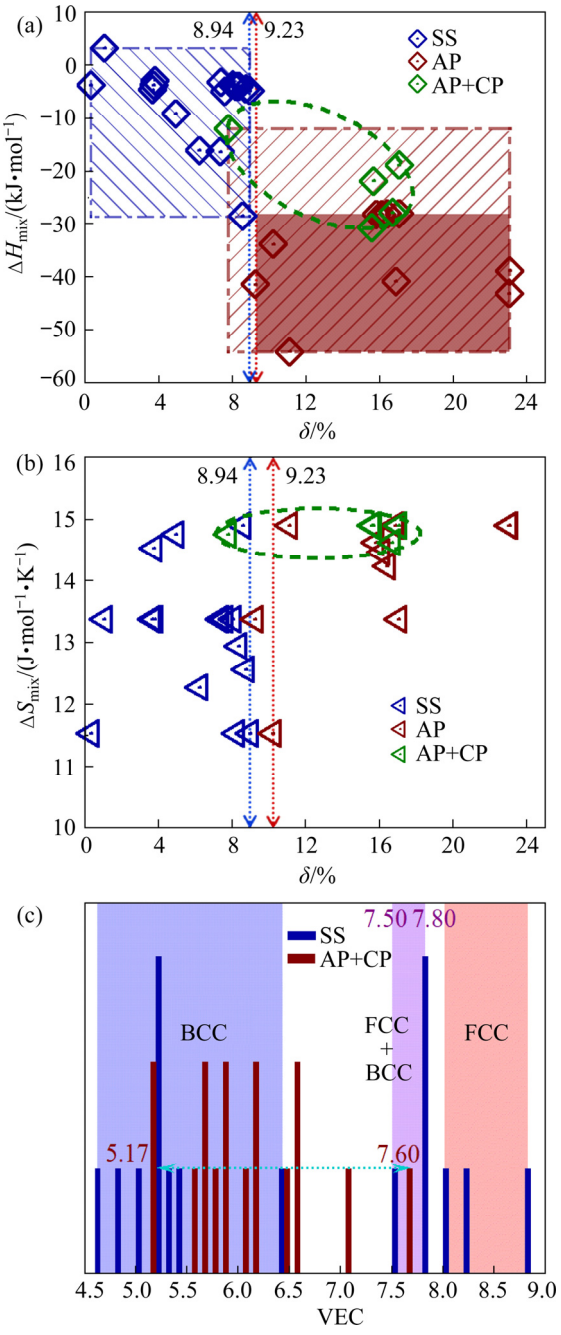

Fig. 9 Relationships of ΔH_{mix}–δ (a) and ΔS_{mix}–δ (b) for HEA powders, and effect of VEC on phase stability in HEA powders (c) (SS: Solid solutions, including different types of solid solutions like mixed FCC and BCC solid solutions; AP: Only amorphous phase; CP: Crystalline phase)

Compared with the solid solution phase, the single amorphous phase is characterized as a higher and wider range of δ (9.23%−23.06%), which depends on a more negative value of ΔH_{mix} (from −54.00 to −28.00 kJ/mol), and a value of ΔS_{mix} ((11.53−14.63) J/(mol·K)). The starting value of δ of the as-milled single amorphous phase formation in HEAs is very close to that of bulk metallic glasses ($\delta \geq 9\%$) [12]. Interestingly, the dual-phase, including crystalline and amorphous phases, could be formed in the intermediate conditions in terms of $\delta \geq 7.78\%$, $\Delta H_{mix} \leq -11.93$ kJ/mol, and $\Delta S_{mix} \leq 14.90$ J/(mol·K), as delineated by the green dash-dotted lines in Figs. 9(a, b). This does not indicate that only these marked regions are the dual-phase alloying products but refer to the conditions where the amount of dual-phase is sufficiently detected by XRD or TEM characterization. Compared with the amorphous phase formation, it is revealed that the solid solution in the as-milled HEA powders can be formed when its δ is smaller, and the corresponding ΔH_{mix} becomes slightly more positive and broader in value range along with similar ΔS_{mix} scope.

It has been reported that solid solutions (including different types of solid solutions) in the as-cast HEAs are only formed under the following conditions, such as $0 \leq \delta \leq 8.5\%$, -22 kJ/mol $\leq \Delta H_{mix} \leq 7$ kJ/mol and 11 J/(mol·K) $\leq \Delta S_{mix} \leq 19.5$ J/(mol·K). Moreover, the region where high-entropy bulk metallic glasses (HE-BMGs) are formed was limited under the conditions of $\delta \geq 9\%$, -28 kJ/mol $\leq \Delta H_{mix} \leq -10$ kJ/mol and 13.38 J/(mol·K) $\leq \Delta S_{mix} \leq$ 14.89 J/(mol·K) [12]. Figure 10 is designed to demonstrate the difference of crucial parameters between the reported as-cast HEAs in Ref. [12] and as-milled HEAs in the present study.

Obviously, δ apparently plays a critical role in distinguishing the formation of solid solution and amorphous phases. The variation span of δ to form the solid solution in the as-milled HEA powders is larger than that of the as-cast ones, as shown in Fig. 10(a). The consistent requirement on the critical δ value to form the solid solution suggests that the essential attributes of the HEAs reflect more acute effects than different existing states. However, the ΔH_{mix} for the as-milled solid solution HEA powders is more negative than that for the as-cast ones, as displayed in Fig. 10(a). However,

the as-milled solid solution HEA powders possess a narrower variation region of ΔS_{mix}, as shown in Fig. 10(b), which is included in the range of solid solution formation of the as-cast HEAs. Thus, compared with the rules of the as-cast HEAs [12], the present experimental data are summarized, and the solid solution in as-milled HEA powders is obtained in a broader distribution of ΔH_{mix}–δ, yet a narrower range of ΔS_{mix}–δ.

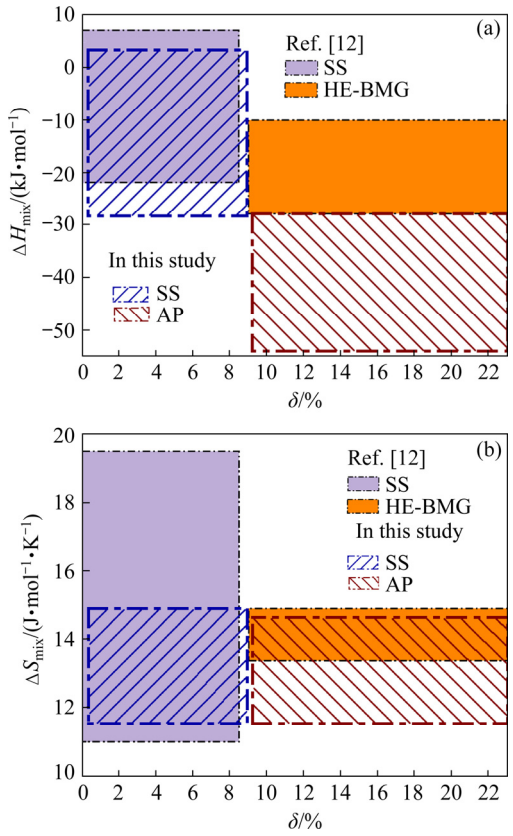

Fig. 10 Criteria comparisons of phase formation in ΔH_{mix}–δ (a) and ΔS_{mix}–δ (b) between reported as-cast HEAs in Ref. [12] and as-milled HEAs in present study

Accordingly, HE-BMGs have a more positive ΔH_{mix} compared to the as-milled amorphous phases. The ΔH_{mix} corresponding to the amorphous phase of the as-milled HEA powders is −54 kJ/mol, which is far more negative than that of the HE-BMGs. Meanwhile, the as-milled HEA amorphous phase possesses a wider variation region of ΔS_{mix} (Fig. 10(b)). In summary, the variation ranges of ΔH_{mix} and ΔS_{mix} of the as-milled amorphous phase with δ become wider than those of the reported HE-BMGs, and both extremes become more negative. It should be emphasized that the parameter range included in the reported literature may be limited due to the insufficient numbers of studied HEA systems used in this work. In the future, we will continue to study different systems of HE-amorphous alloys under similar MA conditions and improve the critical rule of these parameter systems.

Although HEAs have excellent properties and broad application prospects, there is still a lack of a complete theoretical system on the formation rules, which significantly limits the development. As increasing efforts have been made lately to develop new particulate HEAs and investigate their potential applications, the proposed phase formation rules could be updated accordingly in the future to improve adaptability and accessibility. Compared with the study reported in the current literature, the scheme proposed in this work provides a comprehensive strategy for designing HEA powders. It is expected to serve as guidelines for developing novel multi-component powders.

4 Conclusions

(1) The Al10 powders have duplex FCC + BCC solid solution structures. The Hf10 powders consist of an amorphous phase with $HfNi_3$ nanocrystalline as the final MA products.

(2) Both as-milled HEA powders display typical ferromagnetic behaviors. Compared with Hf10 powders, Al10 powders possess a larger M_s of 20.52 A·m^2/kg. It can be explained by the reduced number of down-spins of Mn after the addition of Al. In addition, the coherent interface between FCC and BCC phases with low interface energy facilitates the motion of the magnetic domain.

(3) By calculating parameters of δ, ΔH_{mix}, ΔS_{mix}, and VEC among constituent elements for as-milled HEA powders under similar MA conditions, the rules of forming solid solution and amorphous phase have been proposed. Compared with the phase formation rules of the as-cast HEAs reported earlier, the present study shows that the solid solution in the as-milled HEA powders can be obtained in a broader distribution of ΔH_{mix}–δ. The amorphous phase in the as-milled HEA powders possesses wider distribution of ΔH_{mix}–δ and ΔS_{mix}–δ than that in HE-BMGs, and both extremes become more negative. Moreover, the VEC values of the as-milled HEA powders are entirely consistent with the previous statistical discrimination range of the as-cast HEAs.

Acknowledgments

The authors acknowledge financial supports from the National Natural Science Foundation of China (No. 51971102), the Major Basic Research Projects of Shandong Natural Science Foundation, China (No. ZR2020ZD06), the Open Research Fund of Songshan Lake Materials Laboratory, China (No. 2021SLABFK08), and the Science and Technology Program of University of Jinan, China (No. XKY2117).

References

[1] CANTOR B. Multicomponent high-entropy cantor alloys [J]. Progress in Materials Science, 2021, 120: 100754.

[2] ANDREOLI A F, SHULESHOVA O, WITUSIEWICZ V T, WU Yu-hao, YANG Yan-zhao, IVASHKO O, DIPPEL A, ZIMMERMANN M, NIELSCH K, KABAN I. In situ study of non-equilibrium solidification of CoCrFeNi high-entropy alloy and CrFeNi and CoCrNi ternary suballoys [J]. Acta Materialia, 2021, 212: 116880.

[3] LI Guo-dong, LIU Mao-wen, LYU Shao-yuan, NAKATANI M, ZHENG Rui-xiao, MA Chao-li, LI Qiu-shi, AMEYAMA K. Simultaneously enhanced strength and strain hardening capacity in FeMnCoCr high-entropy alloy via harmonic structure design [J]. Scripta Materialia, 2021, 191: 196−201.

[4] CANTOR B, CHANG I T H, KNIGHT P, VINCENT A J B. Microstructural development in equiatomic multicomponent alloys [J]. Materials Science and Engineering A, 2004, 375/376/377: 213−218.

[5] TORRALBA J M, ALVAREDO P, GARCÍA-JUNCEDA A. High-entropy alloys fabricated via powder metallurgy: A critical review [J]. Powder Metallurgy, 2019, 62: 84−114.

[6] WANG P, HUANG P F, NG F L, SIN W J, LU S L, NAI M L S, DONG Z L, WEI J. Additively manufactured CoCrFeNiMn high-entropy alloy via pre-alloyed powder [J]. Materials and Design, 2019, 168: 107576.

[7] PENG Si-yuan, MOORAJ S, FENG Rui, LIU Liang, REN Jie, LIU Yan-fang, KONG Fan-yue, XIAO Zhi-yu, ZHU Cheng, LIAW P K, CHEN Wen. Additive manufacturing of three-dimensional (3D)-architected CoCrFeNiMn high-entropy alloy with great energy absorption [J]. Scripta Materialia, 2021, 190: 46−51.

[8] ZHANG Lin, SONG Ruo-kang, QU Guo-xin, LU Tong. Effect of nitrogen on microstructure and mechanical properties of $CrMnFeVTi_6$ high entropy alloy [J]. Transactions of Nonferrous Metals Society of China, 2021, 31: 2415−2427.

[9] SHANG Cai-yun, AXINTE E, SUN Jun, LI Xu-ting, LI Peng, DU Jian-wei, QIAO Peng-chao, WANG Yan. CoCrFeNi $(W_{1-x}Mo_x)$ high-entropy alloy coatings with excellent mechanical properties and corrosion resistance prepared by mechanical alloying and hot pressing sintering [J]. Materials & Design, 2017, 117: 193−202.

[10] WANG Nai-ran, WU Bo, WU Wei-long, LI Jiu, GE Chun-hua, DONG YI-fan, ZHANG Lan-xiang, WANG Yan. Microstructure and properties of aluminium-high entropy alloy composites fabricated by mechanical alloying and spark plasma sintering [J]. Materials Today Communications, 2020, 25: 101366.

[11] GUO S, HU Q, NG C, LIU C T. More than entropy in high-entropy alloys: Forming solid solutions or amorphous phase [J]. Intermetallics, 2013, 41: 96−103.

[12] GUO S, LIU C T. Phase stability in high entropy alloys: Formation of solid-solution phase or amorphous phase [J]. Progress in Natural Science: Materials International, 2011, 21: 433−446.

[13] YANG Xiao, ZHANG Yong. Prediction of high-entropy stabilized solid-solution in multi-component alloys [J]. Materials Chemistry and Physics, 2012, 132: 233−238.

[14] FU Jian-xin, CAO Cheng-ming, TONG Wei, PENG Liang-ming. Effect of thermomechanical processing on microstructure and mechanical properties of CoCrFeNiMn high entropy alloy [J]. Transactions of Nonferrous Metals Society of China, 2018, 28: 931−938.

[15] JI Wei, WANG Wei-min, WANG Hao, ZHANG Jin-yong, WANG Yu-cheng, ZHANG Fan, FU Zheng-Yi. Alloying behavior and novel properties of CoCrFeNiMn high-entropy alloy fabricated by mechanical alloying and spark plasma sintering [J]. Intermetallics, 2015, 56: 24−27.

[16] CHEN Qiu-shi, LU Yi-ping, DONG Yong, WANG Tong-min, LI Ting-ju. Effect of minor B addition on microstructure and properties of AlCoCrFeNi multi-component alloy [J]. Transactions of Nonferrous Metals Society of China, 2015, 25: 2958−2964.

[17] XIE Yan-chong, CHENG Hu, TANG Qun-hua, CHEN Wei, CHEN Wei-kun, DAI Ping-qiang. Effects of N addition on microstructure and mechanical properties of CoCrFeNiMn high entropy alloy produced by mechanical alloying and vacuum hot pressing sintering [J]. Intermetallics, 2018, 93: 228−234.

[18] HE Jun-yang, LIU Wei-hong, WANG Hui, WU Yuan, LIU Xing-jiang, NIEH T G, LU Zhao-ping. Effects of Al addition on structural evolution and tensile properties of the FeCoNiCrMn high-entropy alloy system [J]. Acta Materialia, 2014, 62: 105−113.

[19] DEAN S W, ZHANG Y, CHEN G L, GAN C L. Phase change and mechanical behaviors of $Ti_xCoCrFeNiCu_{1-y}Al_y$ high entropy alloys [J]. Journal of ASTM International, 2010, 7: 1−8.

[20] PORTER D A, EASTERLING K E. Phase transformations in metals and alloys [M]. 3rd ed. London: Chapman & Hall, 1992.

[21] GUINIER A. X-ray diffraction in crystals, imperfect crystals and amorphous bodies [M]. 3rd ed. New York: Dover Publication, 1963.

[22] SHARMA S, SURYANARAYANA C. Effect of Nb on the glass-forming ability of mechanically alloyed Fe−Ni−Zr−B alloys [J]. Scripta Materialia, 2008, 58: 508−511.

[23] ZHANG Bin, DUAN Yu-ping, CUI Yu-long, MA Guo-jia, WANG Tong-min, DONG Xing-long. Improving electromagnetic properties of $FeCoNiSi_{0.4}Al_{0.4}$ high entropy alloy powders via their tunable aspect ratio and elemental uniformity [J]. Materials & Design, 2018, 149: 173−183.

[24] PANIGRAHI M, AVAR B. Influence of mechanical alloying on structural, thermal, and magnetic properties of $Fe_{50}Ni_{10}Co_{10}Ti_{10}B_{20}$ high entropy soft magnetic alloy [J]. Journal of Materials Science (Materials in Electronics), 2021, 32: 21124−21134.

[25] LI Zhong, XU Hui, GU Yong, PAN Min-xiang, YU Lin-ye, TAN Xiao-hua, HOU Xue-ling, Correlation between the magnetic properties and phase constitution of

FeCoNi(CuAl)$_{0.8}$Ga$_x$ ($0 \le x \le 0.08$) high-entropy alloys [J]. Journal of Alloys and Compounds, 2018, 746: 285−291.
[26] AVAR B, SIMSEK T, OZCAN S, CHATTOPADHYAY A K, KALKAN B. Structural stability of mechanically alloyed amorphous (FeCoNi)$_{70}$Ti$_{10}$B$_{20}$ under high-temperature and high-pressure [J]. Journal of Alloys and Compounds, 2021, 860: 158528.
[27] NA S M, YOO J H, LAMBERT P K, JONES N J. Room-temperature ferromagnetic transitions and the temperature dependence of magnetic behaviors in FeCoNiCr-based high-entropy alloys [J]. AIP Advances, 2018, 7: 056412.
[28] ZUO Ting-ting, MICHAEL C G, OUYANG Li-zhi, YANG Xiao, CHENG Yong-qiang, FENG Rui, CHEN Shu-ying, LIAW P K, HAWK J A, ZHANG Yong. Tailoring magnetic behavior of CoFeMnNiX (X=Al, Cr, Ga, and Sn) high entropy alloys by metal doping [J]. Acta Materialia, 2017, 130: 10−18.
[29] ZHANG Yong, ZUO Ting-ting, CHENG Yong-qiang, LIAW P K. High-entropy alloys with high saturation magnetization, electrical resistivity, and malleability [J]. Scientific Reports, 2013, 3: 1455.
[30] TSAI M H, FAN A C, WANG H G. Effect of atomic size difference on the type of major intermetallic phase in arc-melted CoCrFeNiX high-entropy alloys [J]. Journal of Alloys and Compounds, 2017, 695: 1479−1487.
[31] SURYANARAYANA C. Mechanical alloying and milling [J]. Progress in Materials Science, 2001, 46: 1−184.
[32] SHANG Cai-yun, AXINTE E, GE Wen-juan, ZHANG Zi-tang, WANG Yan. High-entropy alloy coatings with excellent mechanical, corrosion resistance and magnetic properties prepared by mechanical alloying and hot pressing sintering [J]. Surfaces and Interfaces, 2017, 9: 36−43.
[33] WANG Tao, WANG Ying-zi, WANG Nai-ran, XU Shuai, HAN Zi-han, WANG Yang. Development of a novel (Ni$_{40}$Fe$_{30}$Co$_{20}$Al$_{10}$)$_{90}$Ti$_{10}$ high-entropy alloy with excellent photocatalytic performance [J]. Materials Letters, 2021, 283: 128817.
[34] WANG Wen. The structures and properties of refractory high entropy alloys containing HfCr fabricated by spark plasma sintering [D]. Jinan: University of Jinan, 2019. (in Chinese)
[35] XU Jing, AXINTE E, ZHAO Zheng-feng, WANG Yan. Effect of C and Ce addition on the microstructure and magnetic property of the mechanically alloyed FeSiBAlNi high entropy alloys [J]. Journal of Magnetism and Magnetic Materials, 2016, 414: 59−68.
[36] WANG Wen, LI Bo-yu, ZHAI Si-cheng, XU Juan, NIU Zuo-zhe, XU Jing, WANG Yan. Alloying behavior and properties of FeSiBAlNiCo$_x$ high entropy alloys fabricated by mechanical alloying and spark plasma sintering [J]. Metals and Materials International, 2018, 24: 1112−1119.
[37] XU Jing. Structural control and properties of FeSiBAlNiM (M=C, Co$_x$, Ce, Gd) high entropy alloys [D]. Jinan: University of Jinan, 2016. (in Chinese)
[38] WANG Jian, ZHENG Zhou, XU Jing, WANG Yan. Microstructure and magnetic properties of mechanically alloyed FeSiBAlNi (Nb) high entropy alloys [J]. Journal of Magnetism and Magnetic Materials, 2014, 355: 58−64.
[39] GE Wen-juan, LI Xu-ting, LI Peng, QIAO Peng-chao, DU Jian-wei, XU Shuai, WANG Yan. Microstructures and properties of CuZrAl and CuZrAlTi medium entropy alloys prepared by mechanical alloying and spark plasma sintering [J]. Journal of Iron and Steel Research International, 2017, 24: 448−454.
[40] GE Wen-juan, WANG Ying-zi, SHANG Cai-yuan, ZHANG Zi-tang, WANG Yan. Microstructures and properties of equiatomic CuZr and CuZrAlTiNi bulk alloys fabricated by mechanical alloying and spark plasma sintering [J]. Journal of Materials Science, 2017, 52: 5726−5737.
[41] HAN Zi-han, WANG Dong-zhi, CHEN Xiao-han, SHAO Guo-mang, ZHANG Xi, GE Wen-juan, WANG Yan. Characterization and properties of CuZrAlTiNiSi high entropy alloy coating obtained by mechanical alloying and vacuum hot-pressing sintering [J]. JOM, 2020, 72: 1254−1263.
[42] ZHU Xiao-xiao, ZHOU Xuan, YU Shuai-shuai, WEI Cong-cong, XU Jing, WANG Yan. Effects of annealing on the microstructure and magnetic property of the mechanically alloyed FeSiBAlNiM (M=Co, Cu, Ag) amorphous high entropy alloys [J]. Journal of Magnetism and Magnetic Materials, 2017, 430: 59−64.

机械合金化法制备(CoCrFeNiMn)$_{90}$M$_{10}$ (M=Al, Hf)高熵材料的合金化行为及表征

王乃冉[1]，王守仁[2]，苟晓翔[1]，石泽程[1]，林健翔[1]，刘国强[1]，王 艳[1]

1. 济南大学 材料科学与工程学院，济南 250022；2. 济南大学 机械工程学院，济南 250022

摘 要：研究机械合金化工艺制备 (CoCrFeNiMn)$_{90}$M$_{10}$(M = Al，Hf) 高熵合金粉末的合金化行为和显微组织。(CoCrFeNiMn)$_{90}$Al$_{10}$ 粉末具有双相固溶体结构；而在(CoCrFeNiMn)$_{90}$Hf$_{10}$ 粉末中发现了非晶相及纳米晶 HfNi$_3$ 相。(CoCrFeNiMn)$_{90}$Al$_{10}$ 粉末表现出更好的铁磁性能，这主要归因于双相共格界面易于诱导磁畴的运动。结合我们以前的工作，初步提出球磨态高熵合金粉末中固溶体和非晶相的形成规律。与已报道的铸态高熵合金规律相比，在球磨态高熵合金粉末中形成的固溶体相的混合焓随原子尺寸差变化的范围更宽。此外，高熵合金粉末中非晶相的混合焓或熵随原子尺寸差变化的范围比大块高熵金属玻璃的范围更宽。

关键词：高熵粉末；机械合金化；铁磁性；合金设计；相稳定性

(Edited by Wei-ping CHEN)